Comparison of finite element and fast Fourier transform crystal plasticity solvers for texture prediction

2010 Modelling Simul. Mater. Sci. Eng. 18 085005

(http://iopscience.iop.org/0965-0393/18/8/085005)

Modelling Simul. Mater. Sci. Eng. **18** (2010) 085005 (21pp) doi:10.1088/0965-0393/18/8/085005

Comparison of finite element and fast Fourier transform crystal plasticity solvers for texture prediction

B Liu[1,3], D Raabe[1,3], F Roters[1], P Eisenlohr[1] and R A Lebensohn[2]

[1] Max-Planck-Institut für Eisenforschung, Max-Planck-Str. 1, 40237 Düsseldorf, Germany
[2] MST8-MS G755, Los Alamos National Laboratory, Los Alamos, NM, 87545, USA

E-mail: d.raabe@mpie.de (D Raabe) and b.liu@mpie.de (B Liu)

Received 16 December 2009, in final form 26 July 2010
Published 27 October 2010
Online at stacks.iop.org/MSMSE/18/085005

Abstract

We compare two full-field formulations, i.e. a crystal plasticity fast Fourier transform-based (CPFFT) model and the crystal plasticity finite element model (CPFEM) in terms of the deformation textures predicted by both approaches. Plane-strain compression of a 1024-grain ensemble is simulated with CPFFT and CPFEM to assess the models in terms of their predictions of texture evolution for engineering applications. Different combinations of final textures and strain distributions are obtained with the CPFFT and CPFEM models for this 1024-grain polycrystal. To further understand these different predictions, the correlation between grain rotations and strain gradients is investigated through the simulation of plane-strain compression of bicrystals. Finally, a study of the influence of the initial crystal orientation and the crystallographic neighborhood on grain rotations and grain subdivisions is carried out by means of plane-strain compression simulations of a 64-grain cluster.

(Some figures in this article are in colour only in the electronic version)

1. Introduction

Deformation texture modeling started with the Taylor full-constraints model (1938) [1] using the simplest approximation of equal strain partitioning in a grain aggregate. Owing to this stiff iso-strain formulation and the strong discrepancy between experiments and corresponding predictions this approach was later modified via a global relaxation approximation of some of these strain constraints [2, 3] leading to the relaxed-constraints Taylor models. Later variants, which can be referred to as grain-cluster or grain interaction models, considered local grain

[3] Authors to whom any correspondence should be addressed.

neighborhood relaxations such as Van Houtte's 2-grain-cluster LAMEL model and the modified LAMEL model (ALAMEL model) [4, 5], a grain relaxation model proposed by Evers *et al* [6], and the 8-grain-interaction GIA model of Gottstein and co-workers [7, 8].

Other models cast the mean-field homogenization problem in the form of an ellipsoidal inclusion in an infinite matrix as originally suggested for elastic materials by Eshelby [9]. An extension of this approach to nonlinear constitutive response was suggested by Hill [10]. Molinari *et al* [11] and Lebensohn and Tomé [12] later proposed a self-consistent integral formalism which links effective and grain average stresses and strain rates.

The first full-field crystal plasticity calculations were performed by Peirce *et al* in 1982 [13] using a 2D crystal plasticity finite element method (CPFEM) simulation. The term 'full-field' indicates that both long-range and short-range grain interactions are considered, and the micromechanical fields resolved on a discrete grid. In the CPFEM case a variational solution is achieved for the equilibrium of the forces and the compatibility of the displacements using the principle of virtual work for a volume that is discretized into finite elements. The essential step which renders the deformation kinematics of this approach a crystal plasticity formulation is the fact that the velocity gradient is written in dyadic form (i.e. in terms of the sum of the contributions of the different active slip systems). This reflects the tensorial crystallographic nature of the underlying defects that lead to shear and consequently, to both shape changes (symmetric part) and lattice rotations (skew-symmetric part). These simulations were later extended to a polycrystalline arrangement by Harren *et al* [14, 15] using a 2D set-up with two or three slip systems. Becker performed simulations on the basis of the 12 slip systems of the face-centered cubic (FCC) crystal structure. Using a 3D model for the crystallographic degrees of freedom he calculated channel-die deformation of a columnar polycrystal aggregate [16] and of a single crystal [17]. Since then, CPFEM methods became increasingly popular, particularly to tackle sub-grain scale problems, using meshes with sub-grain resolutions and, in occasions, complex 2D and 3D grain arrangements [18–25].

Following the pioneering work of Suquet and co-workers [26, 27] for linear and nonlinear composites, Lebensohn [28] introduced an alternative full-field crystal plasticity formulation by applying a FFT-based algorithm in conjunction with Green's function method, to solve the governing equations for heterogeneous media (e.g. see Mura [29]). This approximation solves the equilibrium equations under the constraint of strain compatibility for materials with periodic microstructure, which can be generated by periodic repetition of a unit cell. This full-field crystal plasticity fast Fourier transform (CPFFT) approach provides an alternative to the CPFEM model with periodic boundary conditions [30]. In general, for the same spatial resolution, the CPFFT approach is a very efficient alternative compared with CPFEM with periodic boundary conditions. This higher numerical performance of CPFFT is related to the repetitive use of the efficient FFT algorithm, avoiding the time-consuming inversion of large matrices, needed under CPFEM. Although the exact reduction in computation time that it is obtained using CPFFT instead of CPFEM is obviously problem-dependent, it is typically from one to several orders of magnitude [30].

The aim of this work is to analyze and compare the predictions of the CPFFT and CPFEM models for deformation textures of FCC polycrystals. We simulate the rolling texture evolution of a 1024-grain representative volume element (RVE) representing an AA1200 aluminum polycrystal under plane-strain boundary conditions (i.e. an approximation of a rolling process) using the CPFFT and the CPFEM models. To further understand the different predictions of both models, the correlation between grain rotations and strain gradients is next investigated through the simulation of plane-strain compression of bicrystals at different discretization levels. Finally, a study of the influence of the initial crystal orientation and the crystallographic neighborhood on grain rotations and grain subdivisions is carried out by means of plane-strain

compression simulations of a 64-grain RVE with four important orientation components clustered in random order.

2. Comparison of the CPFFT and the CPFEM full-field model formulations

2.1. General

Constitutive models define the relation between the symmetric Cauchy stress tensor $\boldsymbol{\sigma}$ and the strain or strain-rate tensor at a material point level. The material points where the constitutive equations are actually solved can be the set of regular Fourier points, in the case of the CPFFT model; or the Gaussian integration points, in the case of the CPFEM model.

What distinguishes full-field crystal plasticity models from Taylor and grain-cluster approximations is that they solve the equilibrium equations ($\sigma_{ij,j} + f_i^V = 0$) numerically, rather than assuming Taylor-like iso-strain conditions (σ_{ij} is the stress and f_i^V the body force).

The CPFFT model used in this work is based on the Lippmann–Schwinger integral equation for the determination of the strain field in periodic heterogeneous materials [31]. The method was originally developed by Suquet and co-workers [26, 27] as a fast algorithm to compute the elastic and elastoplastic effective and local response of composites, and was later adapted by Lebensohn *et al* [28, 32, 33] to calculate also viscoplastic deformation of complex 3D polycrystalline aggregates.

The CPFEM model used in this comparison is based on the implementation of Kalidindi and Anand [23, 34, 35], which is based on a constitutive viscoplastic law and a phenomenological hardening model.

In this paper we only give a concise comparison of the two models concerning the constitutive formulations, the numerical framework used for solving the equilibrium equations. The same crystal plasticity constitutive equation and hardening law of the two models are briefly mentioned. More details are given in [33, 36].

2.2. CPFFT model: theoretical framework

The method relies on the fact that the local response of a heterogeneous medium can be obtained from convolution integrals between Green functions associated with the micromechanical fields of an equivalent linear homogeneous medium with eigenstrains, and a polarization field in which one collects the actual heterogeneity of the medium, including any possible nonlinearity of the local mechanical behavior. For periodic media, Fourier transforms can be used to reduce these convolution integrals in real space to a simple product in Fourier space between the polarization field and an appropriate kernel function. The FFT algorithm can be used to transform the polarization field into Fourier space and to anti-transform the aforementioned product back to real space. However, since the actual polarization field depends precisely on the *a priori* unknown mechanical fields, and the viscoplastic constitutive behavior determines a strong mechanical contrast in local properties, an iterative scheme based on augmented Lagrangians [27] needs to be implemented to obtain, upon convergence, a compatible strain-rate field and an equilibrated stress field, related to each other through the nonlinear constitutive equation.

The periodic unit cell representing the polycrystal is discretized into $N_1 \times N_2 \times N_3$ Fourier points, determining a regular grid in the Cartesian space $\{\boldsymbol{x}^d\}$ and a corresponding grid in Fourier space $\{\boldsymbol{\xi}^d\}$. A velocity gradient $V_{i,j}$ that can be decomposed into a symmetric strain-rate and a antisymmetric rotation rate, i.e. $V_{i,j} = \dot{E}_{ij} + \dot{\Omega}_{ij}$, is imposed to the unit cell. The local strain-rate field $\dot{\varepsilon}_{ij}(\boldsymbol{x}) = \frac{1}{2}(v_{i,j}(\boldsymbol{x}) + v_{j,i}(\boldsymbol{x}))$ is a function of the local velocity field,

and both can be split into its average and a fluctuation term: $\dot{\varepsilon}_{ij}(v_k(\boldsymbol{x})) = \dot{E}_{ij} + \tilde{\dot{\varepsilon}}_{ij}(\tilde{v}_k(\boldsymbol{x}))$, where $v_i(\boldsymbol{x}) = \dot{E}_{ij}x_j + \tilde{v}_i(\boldsymbol{x})$. The velocity fluctuation field $\tilde{v}_k(\boldsymbol{x})$ has to be periodic across the boundary of the unit cell, and the traction field antiperiodic, to meet equilibrium on the boundary between contiguous unit cells.

The local constitutive relation between the strain rate $\dot{\varepsilon}_{ij}(\boldsymbol{x})$ and the deviatoric stress $\sigma'_{ij}(\boldsymbol{x})$ is given by the rate-sensitivity equation for single-crystal plasticity:

$$\dot{\varepsilon}_{ij}(\boldsymbol{x}) = \sum_{s=1}^{N_s} m^s_{ij}(\boldsymbol{x})\dot{\gamma}^s(\boldsymbol{x}) = \dot{\gamma}_o \sum_{s=1}^{N_s} m^s_{ij}(\boldsymbol{x}) \left(\frac{|m^s(\boldsymbol{x}) : \sigma'(\boldsymbol{x})|}{\tau^s_c(\boldsymbol{x})} \right)^n \operatorname{sgn}(m^s(\boldsymbol{x}) : \sigma'(\boldsymbol{x})), \tag{2.2.1}$$

where m^s_{ij}, $\dot{\gamma}^s$ and τ^s_c are, respectively, the symmetric Schmid tensor, the shear rate and the threshold stress of slip system (s); n is the rate-sensitivity exponent, $\dot{\gamma}_o$ is the reference shear rate and N_s is the number of slip systems in the single crystal. With $p(\boldsymbol{x})$ being the hydrostatic pressure field, the Cauchy stress field can be written as

$$\sigma_{ij}(\boldsymbol{x}) = L^o_{ijkl}\dot{\varepsilon}_{kl}(\boldsymbol{x}) + \varphi_{ij}(\boldsymbol{x}) - p(\boldsymbol{x})\delta_{ij}. \tag{2.2.2}$$

The polarization field $\varphi_{ij}(\boldsymbol{x})$ is given by

$$\varphi_{ij}(\boldsymbol{x}) = \sigma'_{ij}(\boldsymbol{x}) - L^o_{ijkl}\dot{\varepsilon}_{kl}(\boldsymbol{x}), \tag{2.2.3}$$

where L^o is the stiffness of a linear reference medium (note that the particular choice of L^o changes the rate of convergence of the numerical algorithm but not the converged results). Combining equation (2.2.2) with the equilibrium and the incompressibility conditions gives

$$\begin{vmatrix} L^o_{ijkl}v_{k,lj}(\boldsymbol{x}) + \varphi_{ij,j}(\boldsymbol{x}) - p_{,i}(\boldsymbol{x}) = 0, \\ v_{k,k}(\boldsymbol{x}) = 0. \end{vmatrix} \tag{2.2.4}$$

The auxiliary system for the determination of Green's functions is then given by

$$\begin{vmatrix} L^o_{ijkl}G_{km,lj}(\boldsymbol{x} - \boldsymbol{x}') + H_{m,i}(\boldsymbol{x} - \boldsymbol{x}') + \delta_{im}\delta(\boldsymbol{x} - \boldsymbol{x}') = 0, \\ G_{km,k}(\boldsymbol{x} - \boldsymbol{x}') = 0. \end{vmatrix} \tag{2.2.5}$$

After some manipulation, the convolution integrals that give the velocity and velocity-gradient deviation fields are

$$\tilde{v}_k(\boldsymbol{x}) = \int_{\mathrm{R}^3} \mathrm{G}_{ki,j}(\boldsymbol{x} - \boldsymbol{x}')\varphi_{ij}(\boldsymbol{x}')\,\mathrm{d}\boldsymbol{x}', \tag{2.2.6}$$

$$\tilde{v}_{i,j}(\boldsymbol{x}) = \int_{\mathrm{R}^3} \mathrm{G}_{ik,jl}(\boldsymbol{x} - \boldsymbol{x}')\varphi_{kl}(\boldsymbol{x}')\,\mathrm{d}\boldsymbol{x}', \tag{2.2.7}$$

Convolution integrals in direct space are products in Fourier space:

$$\hat{\tilde{v}}_k(\boldsymbol{\xi}) = (-i\xi_j)\hat{G}_{ki}(\boldsymbol{\xi})\hat{\varphi}_{ij}(\boldsymbol{\xi}), \tag{2.2.8}$$

$$\hat{\tilde{v}}_{i,j}(\boldsymbol{\xi}) = \hat{\Gamma}_{ijkl}(\boldsymbol{\xi})\hat{\varphi}_{kl}(\boldsymbol{\xi}), \tag{2.2.9}$$

where the symbol '$\hat{}$' indicates a Fourier transform. The Green operator in equation (2.2.9) is defined as $\Gamma_{ijkl} = G_{ik,jl}$. The tensors $\hat{G}_{ij}(\boldsymbol{\xi})$ and $\hat{\Gamma}_{ijkl}(\boldsymbol{\xi})$ can be calculated by taking Fourier transform to system (2.2.5) (see [33] for details), resulting in

$$\hat{G}_{ij}(\boldsymbol{\xi}) = A^{-1}_{ij}(\boldsymbol{\xi}), \tag{2.2.10}$$

$$\hat{\Gamma}_{ijkl}(\boldsymbol{\xi}) = -\xi_j\xi_l\hat{G}_{ik}(\boldsymbol{\xi}), \tag{2.2.11}$$

where $A_{ik}(\boldsymbol{\xi}) = \xi_l\xi_j L^o_{ijkl}$.

2.3. CPFFT model: numerical algorithm

Assigning initial values to the strain-rate field in the regular grid $\{\boldsymbol{x}^{\boldsymbol{d}}\}$ (e.g. using a 'Taylor' guess: $\tilde{\dot{\varepsilon}}_{ij}^{(o)}(\boldsymbol{x}^{\boldsymbol{d}}) = 0 \Rightarrow \dot{\varepsilon}_{ij}^{(o)}(\boldsymbol{x}^{\boldsymbol{d}}) = \dot{E}_{ij}$), and computing the corresponding stress field $\sigma_{ij}^{\prime(o)}(\boldsymbol{x}^{\boldsymbol{d}})$ from the local constitutive relation (equation (2.2.1)), gives an initial guess for the polarization field in direct space $\varphi_{ij}^{(o)}(\boldsymbol{x}^{\boldsymbol{d}})$ (equation (2.2.3)), and its Fourier transform $\hat{\varphi}_{ij}^{(o)}(\boldsymbol{\xi}^{\boldsymbol{d}})$.

Choosing the initial guess of an auxiliary stress field λ_{ij} (i.e. the Lagrange multiplier associated with the compatibility constraints) as $\lambda_{ij}^{(o)}(\boldsymbol{x}^{\boldsymbol{d}}) = \sigma^{\prime(o)}_{ij}(\boldsymbol{x}^{\boldsymbol{d}})$, the iterative procedure based on augmented Lagrangians [27] reads as follows.

With the polarization field after iteration n being known, the $n+1$th iteration starts by computing the new guess for the kinematically admissible strain-rate deviation field:

$$\hat{\tilde{d}}_{ij}^{(n+1)}(\boldsymbol{\xi}^{\boldsymbol{d}}) = -\hat{\Gamma}^{\mathrm{sym}}_{ijkl}(\boldsymbol{\xi}^{\boldsymbol{d}})\hat{\varphi}^{(n)}_{kl}(\boldsymbol{\xi}^{\boldsymbol{d}}), \qquad \forall \boldsymbol{\xi}^{\boldsymbol{d}} \neq 0; \quad \text{and} \quad \hat{\tilde{d}}_{ij}^{(n+1)}(\mathbf{0}) = 0, \tag{2.3.1}$$

where $\hat{\Gamma}^{\mathrm{sym}}_{ijkl}$ is the Green operator (equation (2.2.11)), appropriately symmetrized. The corresponding field in real space is thus obtained by application of the inverse FFT, i.e.

$$\tilde{d}_{ij}^{(n+1)}(\boldsymbol{x}^{\boldsymbol{d}}) = \mathrm{FFT}^{-1}[\hat{\tilde{d}}_{ij}^{(n+1)}(\boldsymbol{\xi}^{\boldsymbol{d}})] \tag{2.3.2}$$

and the new guess for the deviatoric stress field $\sigma_{ij}^{\prime(n+1)}$ is calculated from the set of nonlinear equations (omitting subindices):

$$\begin{aligned}\sigma^{\prime(n+1)}(\boldsymbol{x}^{\boldsymbol{d}}) + L^{o} : \dot{\gamma}_o \sum_{s=1}^{N_s} m^s(\boldsymbol{x}^{\boldsymbol{d}}) \left(\frac{m^s(\boldsymbol{x}^{\boldsymbol{d}}) : \sigma^{\prime(n+1)}(\boldsymbol{x}^{\boldsymbol{d}})}{\tau_c^s(\boldsymbol{x}^{\boldsymbol{d}})} \right)^n \times \mathrm{sgn}(m^s(\boldsymbol{x}^{\boldsymbol{d}}) : \sigma^{\prime(n+1)}(\boldsymbol{x}^{\boldsymbol{d}})) \\ = \lambda^{(n)}(\boldsymbol{x}^{\boldsymbol{d}}) + L^{o} : (\dot{E} + \tilde{d}^{(n+1)}(\boldsymbol{x}^{\boldsymbol{d}}))\end{aligned} \tag{2.3.3}$$

which can be efficiently solved by Newton–Raphson. The iteration is completed with the calculation of the new guess of the Lagrange multiplier field:

$$\lambda^{(n+1)}(\boldsymbol{x}^{\boldsymbol{d}}) = \lambda^{(n)}(\boldsymbol{x}^{\boldsymbol{d}}) + L^{o} : (\tilde{\varepsilon}^{(n+1)}(\boldsymbol{x}^{\boldsymbol{d}}) - \tilde{\mathrm{d}}^{(n+1)}(\boldsymbol{x}^{\boldsymbol{d}})). \tag{2.3.4}$$

Equations (2.3.3) and (2.3.4) in general guarantee the convergence of $\dot{\varepsilon}_{ij}$ and σ'_{ij} toward d_{ij} and λ_{ij}, respectively.

Upon convergence, the micromechanical fields (velocity, velocity gradient and stress fields) are assumed to be constant in a time interval Δt. The microstructure, e.g. the crystallographic orientation and the threshold stresses for slip, can be then updated for each Fourier point after each time increment. In particular, the new position of the Fourier points can be determined as $x_i = X_i + v_i \Delta t = X_i + (\dot{E}_{ij} x_j + \tilde{v}_i)\Delta t$. This update, however, would destroy the regularity of the Fourier grid after the very first time increment. Therefore, in what follows we use a simplified update scheme, neglecting the velocity fluctuation term: $x_i = X_i + \dot{E}_{ij} x_j \Delta t$. This results in an evolving regular Fourier grid, in which the distances between adjacent points change after each increment following the average stretching prescribed by the macroscopic deformation. The implications of this simplified updating scheme were discussed in [30] and, for the particular case of plane-strain of fcc materials, it was shown that only minor differences should be expected with respect to the more accurate morphologic evolution considering the velocity fluctuation term.

2.4. CPFEM model: theoretical framework

FEM models are based on the variational solution of the equilibrium of the forces using a weak form. Based on the principle of virtual work the basic equation reads

$$\int_V \sigma_{ij} \delta \dot{\epsilon}_{ij} \, \mathrm{d}V = \int_V f_i^V \delta v_i \, \mathrm{d}V + \int_S f_i^S \delta v_i \, \mathrm{d}S, \tag{2.4.1}$$

where f_i^V is the body force, f_i^S is the surface traction, δv_i is the virtual velocity field, $\delta\dot{\epsilon}_{ij}$ is the virtual strain rate, $\dot{\epsilon}_{ij} = \frac{1}{2}(v_{i,j} + v_{j,i})$, V is the current volume and S is the surface bounding this volume.

The entire sample volume under consideration is discretized into elements, which is the reason why FEM is especially well suited for arbitrary geometries. The integrals in equation (2.4.1) can be split into integrals over the individual elements. That is each integral is split into a sum over N integrals, with N being the number of elements in the mesh. As the elements used in FEM have simple regular shapes, the individual element integrals can be easily evaluated numerically using, e.g., Gaussian quadrature.

In order to solve equation (2.4.1) the Cauchy stress σ_{ij} has to be calculated. In CPFEM models this is done via the generalized Hooke's law:

$$\sigma_{ij} = \frac{1}{J} F^{\mathrm{e}}_{ik} S_{kl} F^{\mathrm{e}}_{jl} \qquad \text{and} \qquad S_{ij} = C_{ijkl} \epsilon^{G,*}_{kl}, \tag{2.4.2}$$

where F^{e}_{ij} is the elastic part of deformation gradient F_{ij}, $J = \det(\boldsymbol{F}^{\mathrm{e}})$, S_{ij} is the second Piola–Kirchhoff stress, that is work conjugate to the elastic Green–Lagrange strain $\epsilon^{G,*}_{ij} = \frac{1}{2}(F^{\mathrm{e}}_{ki} F^{\mathrm{e}}_{kj} - \delta_{ij})$ and C_{ijkl} is the constant fourth-order elastic stiffness tensor. F^{e}_{ij} is calculated from the multiplicative decomposition of F_{ij}

$$F_{ij} = F^{\mathrm{e}}_{ik} F^{\mathrm{p}}_{kj}. \tag{2.4.3}$$

In order to do this one has to know the plastic deformation gradient F^{p}_{ij}, which evolves according to

$$\dot{F}^{\mathrm{p}}_{ij} = v^{\mathrm{p}}_{i,j} F^{\mathrm{p}}_{ij}. \tag{2.4.4}$$

In the CPFEM the plastic velocity gradient $v^{\mathrm{p}}_{i,j}$ is calculated from the slip rates $\dot{\gamma}^s$ on all active slip systems s:

$$v^{\mathrm{p}}_{i,j} = \sum_{s=1}^{N_s} \dot{\gamma}^s m^s_i n^s_j. \tag{2.4.5}$$

where m^s_i is the slip direction and n^s_i the slip plane normal of slip system s.

2.5. CPFEM model: numerical algorithm

Crystal plasticity material models can be directly implemented into commercial FEM solvers in the form of user subroutines, e.g. HYPELA2 in MSC.Marc or UMAT/VUMAT in Abaqus. For implicit solvers the purpose of a material model is twofold: first, the stress σ_{ij} is calculated which is required to reach the final deformation gradient F_{ij}; second, the Jacobian matrix, $J_{ijkl} = \mathrm{d}\sigma_{ij}/\mathrm{d}\epsilon^G_{jk}$, is calculated, where ϵ^G_{ij} is the total Green–Lagrange strain.

The stress calculation is implemented using a predictor–corrector scheme. Figure 1 visualizes the set-up of the clockwise loop of calculations to be performed. With an initial guess $v^{\mathrm{p,guess}}_{i,j}$, the prediction $v^{\mathrm{p}}_{i,j}$ is updated using a Newton–Raphson scheme until convergence is reached, i.e. the difference between $v^{\mathrm{p,guess}}_{i,j}$ and $v^{\mathrm{p}}_{i,j}$ falls below a prescribed threshold.

The Jacobian matrix is calculated numerically by perturbing the deformation gradient F_{ij} and determining the new resulting stress σ_{ij}.

2.6. Constitutive equation and hardening law

Both crystal plasticity models relate the shear rate on a system s to the stress acting on the system and the critical threshold stress (critical shear stress) of this system through a viscoplastic form

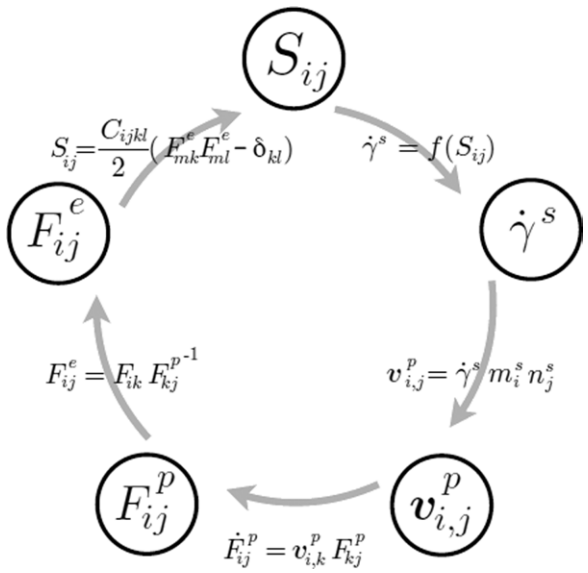

Figure 1. Clockwise loop of calculations during stress determination. Symbols: S_{ij} second Piola–Kirchhoff stress, $\dot{\gamma}^s$ shear rate, $v^{\mathrm{p}}_{i,j}$ plastic velocity gradient, m^s_i slip direction, n^s_i slip plane normal, F^{p}_{ij} plastic deformation gradient, F^{e}_{ij} elastic deformation gradient, C_{ijkl} elasticity tensor, δ_{ij} Kronecker delta.

according to

$$\dot{\gamma}^s = \dot{\gamma}_0 \left| \frac{\tau^s}{\tau^s_c} \right|^{1/m} \mathrm{sgn}(\tau^s), \tag{2.6.1}$$

where τ^s is the resolved shear stress on slip system s and m ($m = 0.1$) is the rate-sensitivity parameter, which is the reciprocal of n in equation (2.2.1).

For describing the evolution of the critical shear stress as a function of the accumulated preceding shears, both models use the hardening law based on the work of Brown *et al* [37].

$$\dot{\tau}^s_c = \sum_{s'} q^{ss'} h^{s'} |\dot{\gamma}^{s'}| \qquad \text{and} \qquad h^{s'} = h_0 \left(1 - \frac{\tau^{s'}_c}{\tau_s} \right)^a, \tag{2.6.2}$$

where $q^{ss'}$ ($q^{ss'} \equiv 1.0$) is the ratio matrix of latent hardening rate to self-hardening rate, τ_s ($\tau_s = 90$ MPa) is the saturation shear stress, h_0 ($h_0 = 400$ MPa) and a ($a = 2.25$) are constant parameters. The stress–strain curves calculated by both models are shown in figure 2.

3. Statistical texture evolution predicted by CPFFT and CPFEM: results and discussion

3.1. Starting texture and orientation mapping

The simulations started with a typical recrystallization texture of FCC metals containing a Cube orientation $(0°, 0°, 0°)$[4] with scatter about the rolling direction (RD) from Cube toward Goss $(0°, 45°, 0°)$, figure 3 left. The corresponding orientation distribution function (ODF) is constructed from 1024 equally weighted orientations [38]. The same spatial configuration of 1024 grains (figure 3 right) is used as starting configuration for both, the CPFEM and CPFFT simulations.

[4] Bunge–Euler notation.

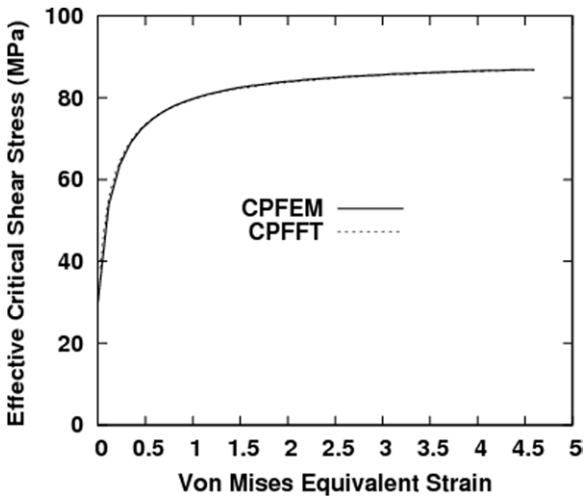

Figure 2. Evolution of the critical shear stress as a function of deformation in the two models.

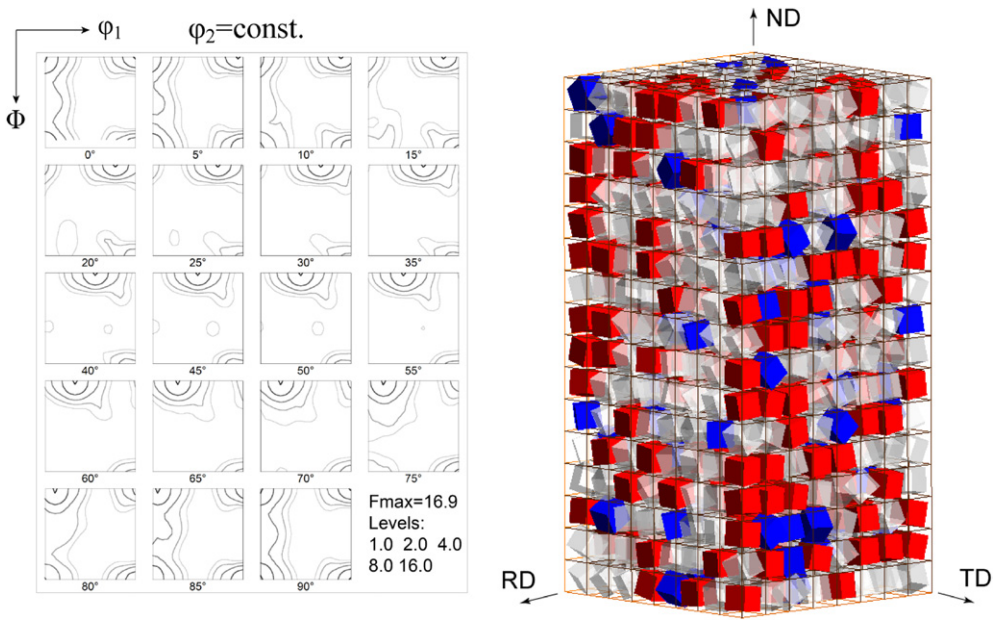

Figure 3. Initial texture and orientation mapping for the CPFFT and CPFEM simulations. The starting texture contains a Cube orientation (0°, 0°, 0°) with some scatter about the RD from the Cube toward the Goss (0°, 45°, 0°). Small cube symbols represent the crystallographic orientations. Red and blue colors indicate orientations within a 15° misorientation to Cube and Goss, respectively. The intermediate orientations are transparent.

The figure shows the unit cell and the sample reference frame, and the cube symbols represent the crystallographic orientations, which have been rotated about the sample axes accordingly. Red and blue colors indicate orientations that are within 15° misorientation to Cube and Goss, respectively. The other intermediate orientations are transparent. For the texture simulations the orientations are mapped onto the integration points for the CPFEM model and on the

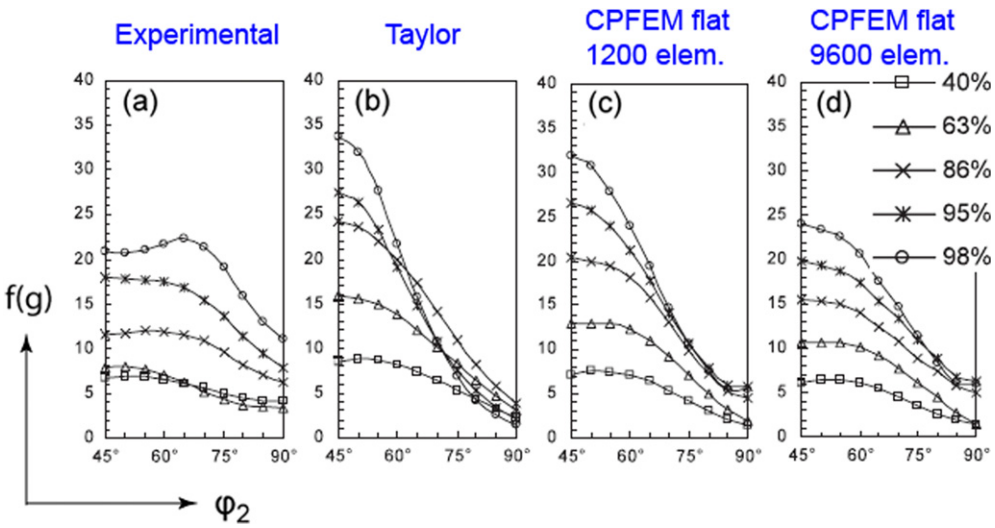

Figure 4. Rolling texture β-fiber, after Li *et al* [39]: (*a*) experimental results of aluminum alloys AA1200, (*b*) Taylor model, (*c*) CPFEM with flat surface boundary conditions (1200 elements, 1200 grains), (*d*) CPFEM with flat surface boundary conditions (9600 elements, 1200 grains).

Fourier points for the CPFFT model. The sample size and geometry ($8 \times 8 \times 16$) were chosen to approximate previous CPFEM texture simulations in the literature [39] which used 1200 grains. Also, the unit cell size and discretization was made compatible with the FFT algorithm. In the present CPFFT implementation, the FFT is performed by adopting the algorithm from [40], which requires that the number of Fourier points to be a power of two along each dimension.

3.2. Analysis of the predicted texture fibers and strain distributions

In what follows, the ODFs are calculated from the discrete orientations of the 1024-grain ensemble using spherical harmonics with a 7° Gaussian smoothing. This method was also employed in previous works used for comparison [5, 39, 41]. First, we compared the β-fiber predictions of our CPFEM calculations (periodic boundary conditions) with earlier ones (flat surface boundary conditions) by Li *et al* [39]. The overall CPFEM texture simulations with all surfaces flat, figure 4(*c*), yield predictions close to those of the Taylor model, figure 4(*b*), while the use of periodic boundary conditions, figure 5(*a*), allows the crystals more freedom during deformation and thus the results show more deviations to those of the Taylor model.

For comparison purposes, the CPFEM and CPFFT textures are presented in terms of β-fiber plots, which reveal an increase in intensity of the stable rolling orientations (copper (90°, 35°, 45°), S (59°, 37°, 63°) and brass (35°, 45°, 0°)), figures 5(*a*)–(*c*); and Cube-RD fiber plots, figures 6(*a*)–(*c*), which show a decrease in the density of the starting orientations, namely a drastic decay of the Cube orientation and the metastability of the Goss orientation. In the CPFFT simulations the originally Cube oriented grains show higher rotation rates away from their initial orientation, but further on, the reorientation of these grains toward the stable plane-strain orientations (copper, S, brass) becomes slower (figures 5(*b*) and 6(*b*)) than in the corresponding CPFEM simulations (figures 5(*a*) and 6(*a*)). The CPFFT textures with different resolutions are nearly the same, figures 5(*b*), (*c*) and 6(*b*), (*c*), while this is not the case with CPFEM, figures 4(*c*) and (*d*). As the number of elements increased from 1 to 8

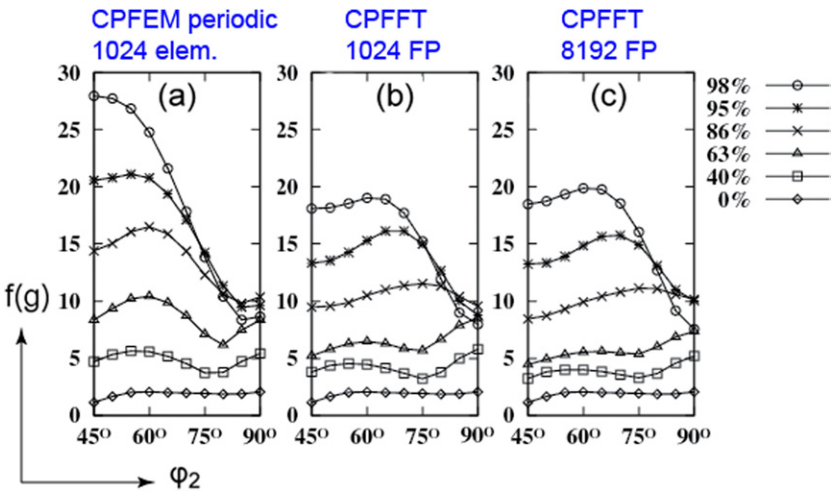

Figure 5. Rolling texture β-fiber, this work: (*a*) CPFEM with periodic boundary conditions (1024 elements, 1024 grains), (*b*) CPFFT (1024 Fourier points, 1024 grains), (*c*) CPFFT (8192 Fourier points, 1024 grains).

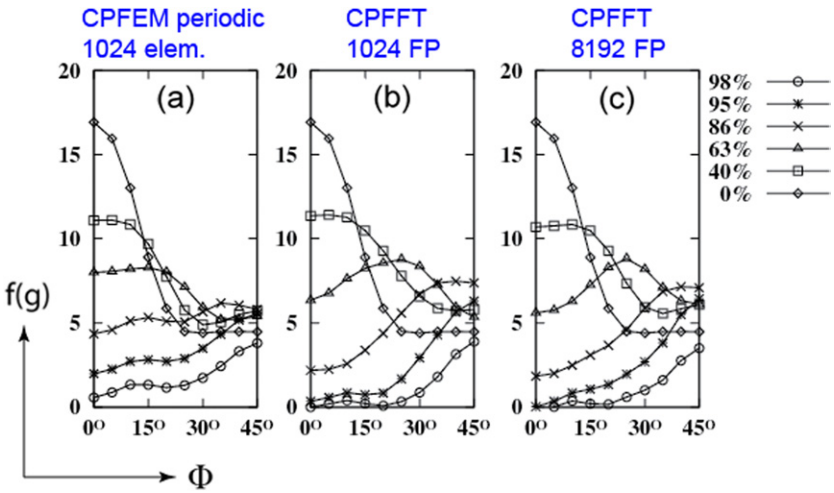

Figure 6. Rolling texture Cube-RD fiber: (*a*) CPFEM with periodic boundary conditions (1024 elements, 1024 grains), (*b*) CPFFT (1024 Fourier points, 1024 grains), (*c*) CPFFT (8192 Fourier points, 1024 grains).

per grain, a substantial drop in intensity of the copper component is observed, which makes the results deviate from the Taylor model calculations, figure 4(*b*), closer to the experimental results, figure 4(*a*). For the CPFFT simulation, strikingly, even at low resolution, the calculated β-fibers (figure 6(*b*)) match well the experimental results (figure 4(*a*)).

The strain distributions of the CPFEM and CPFFT simulations are given in figure 7. All the strain components have broader fluctuation ranges in the CPFFT simulations than in the CPFEM simulation. In the CPFFT case, with increasing resolution (1 Fourier point to 8 Fourier points per grain), the strain distributions become smoother especially for strain component

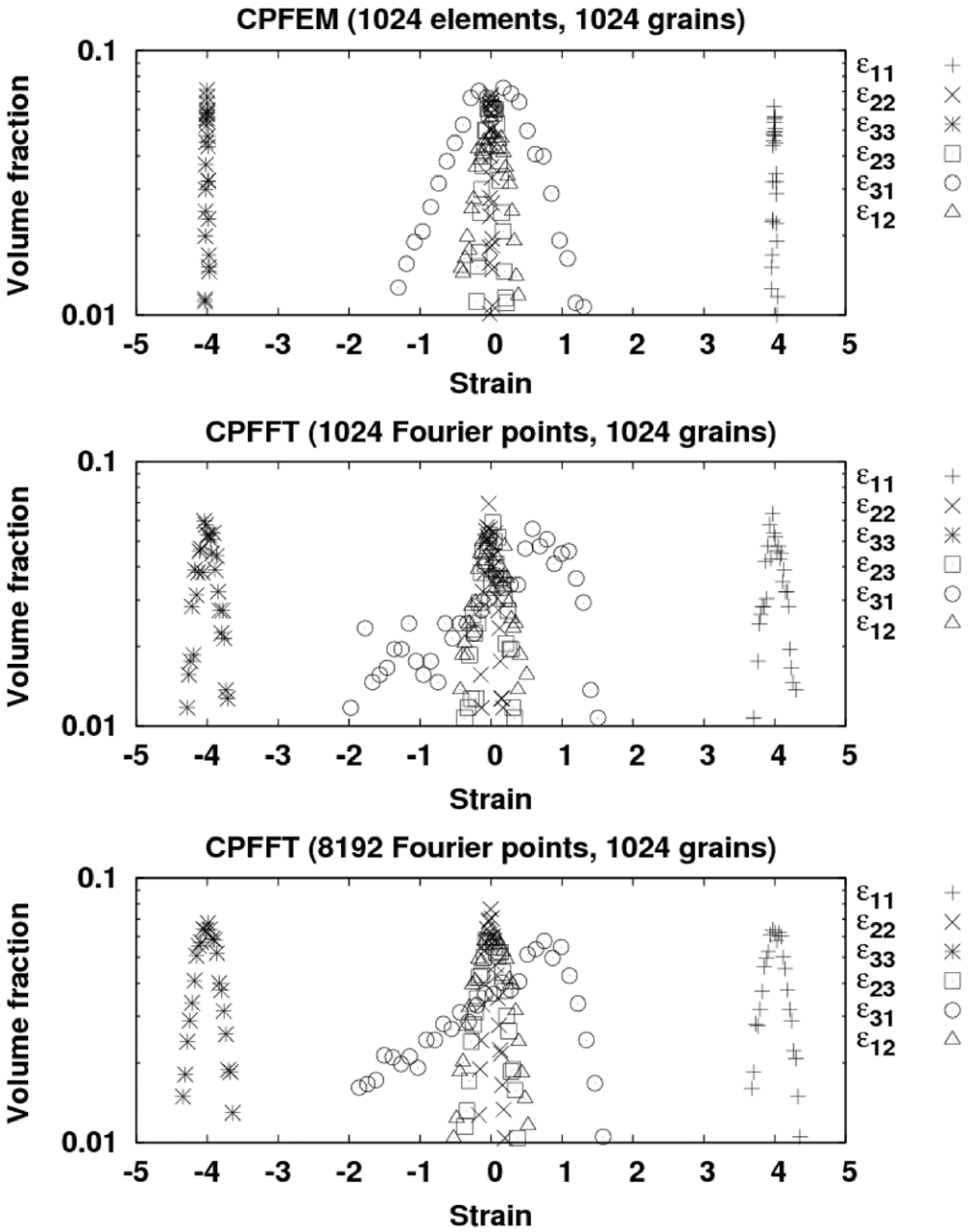

Figure 7. Strain distributions after plane-strain compression at 98% thickness reduction: CPFEM with periodic boundary conditions (1024 elements, 1024 grains), CPFFT (1024 Fourier points, 1024 grains), CPFFT (8192 Fourier points, 1024 grains).

ϵ_{31}, but the distribution widths for all strain components hardly change. With the same initial configuration and boundary conditions, using the same crystal plasticity constitutive equation and hardening law, the CPFEM and CPFFT simulations give different combinations of orientation and strain distributions.

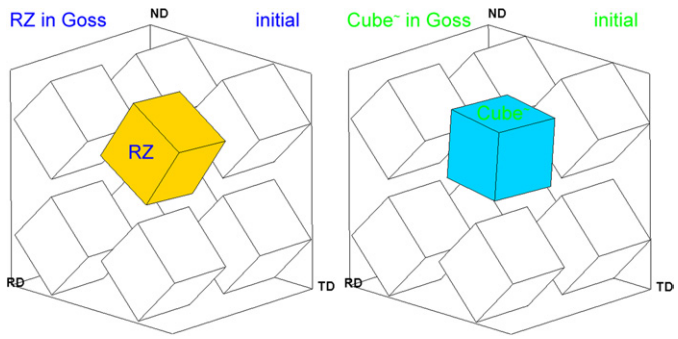

Figure 8. Initial configurations of the bicrystals.

The above comparison between the predictions of both models leads to the following questions:

- What causes the different textures and strain distributions as predicted by the two models?
- Why increasing the resolution has almost no effect on the textures and strain distributions predicted with CPFFT, but strongly affects the CPFEM results?

To start addressing these issues, let us first note that texture evolution is closely connected to strain distribution, in such a way that a sharp rolling texture with the copper component dominating the β-fiber corresponds to a strain distribution that does not deviate much from the macroscopic strain state. On the other hand, the local strain deviations from the macroscopic state have to be balanced by the surrounding material. In other words, how much the local strain can deviate from the average depends on the how large are the strain gradients that can be accommodated. Thus, from figure 7, it can be concluded that, on average, the strain gradients are smaller and more sensitive to mesh refinement in the CPFEM simulations compared with the CPFFT case.

With these in mind, next section presents a study of the strain gradients predicted by CPFEM and CPFFT in the case of bicrystals, including the analysis of the role played, respectively, by the FE mesh and the Fourier grid refinements.

4. Strain gradients predicted by CPFFT and CPFEM for bicrystals: results and discussion

To investigate the difference between the CPFFT and CPFEM models in solving strain gradients, we simulate plane-strain compression of two bicystals at 90% thickness reduction. The two grains of the first bicrystal are assigned with the RZ orientation (32°, 85°, 85°) [42] and the Goss orientation (0°, 45°, 0°). In the periodic sense, the RZ grain is surrounded by the Goss grain, figure 8(left). The second bicrystal is different from the first one in the way that the center grain is assigned with an initial orientation that is the Cube orientation (0°, 0°, 0°) rotated 5° about ND and 5° about RD, which will be referred to as 'Cube˜' (5°, 5°, 0°) from now on, figure 8(right). The introduction of a RZ grain or a Cube˜ grain surrounded by a Goss matrix gives relative high and low strain gradients across the bicrystals, respectively. The simulations were run with different resolutions: 1, 8, 64, 512 Fourier points or finite elements for the RZ and Cube˜ grains and 1×7, 8×7, 64×7, 512×7 Fourier points or finite elements for the surrounding Goss grain.

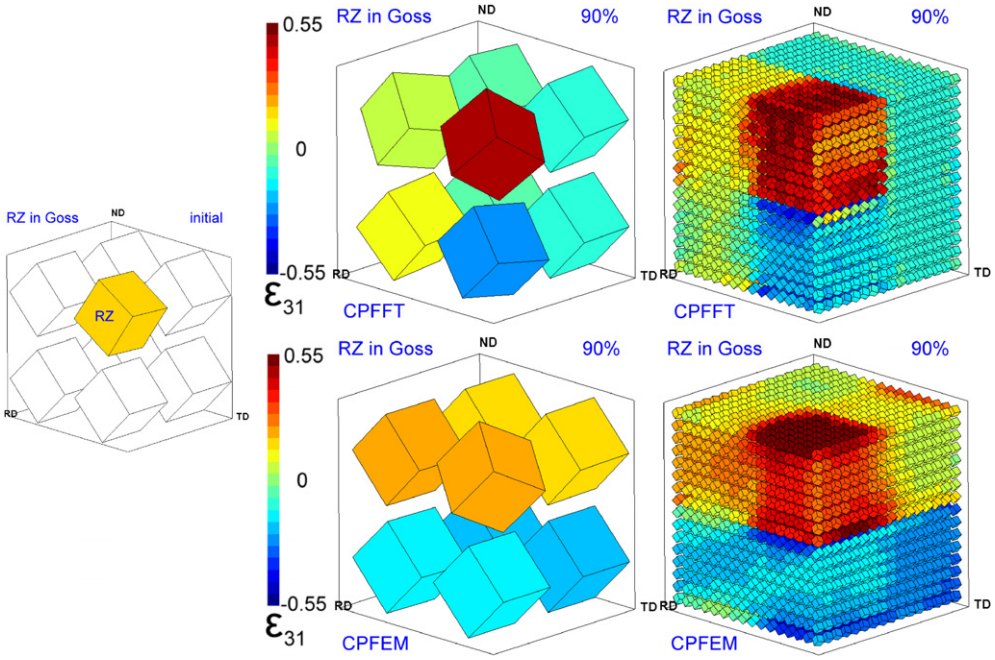

Figure 9. Final crystallographic orientations and strain states on the material points after plane-strain compression of a bicrystal (RZ in Goss) at 90% thickness reduction. The cube symbols are rotated according to the final orientations, and colored according to the values of strain component ϵ_{31}. The results correspond to the simulations run at the lowest resolution (1 Fourier point or element in the RZ grain and 1×7 Fourier points or elements in the Goss grain) (left) and at the highest resolution (512 Fourier points or elements in the RZ grain and 512×7 Fourier points or elements in the Goss grain) (right).

The results of these bicrystal simulations are presented in the following way:

- The final local crystallographic orientations are represented by the rotations of the small cubes, and the values of local shear strain component ϵ_{31} are represented by the color of those cubes. (In this paper RD, TD and ND of the sample are identified with directions 1, 2 and 3, respectively.) Using this convention the results of the simulations run with the lowest and highest resolutions are presented in figure 9 for the 'RZ-in-Goss' bicrystal, and in figure 11 for the 'Cube$^{\sim}$-in-Goss' case.
- The grain averages of ϵ_{31} are plotted with the consideration of the different volume fractions of the crystals (for the RZ and Cube$^{\sim}$ grains: $\epsilon_{31} \times 1$, for the Goss grain: $\epsilon_{31} \times 7$). The strain plots obtained with different resolutions are presented in figure 10 for the RZ-in-Goss, and in figure 12 for Cube$^{\sim}$-in-Goss cases.

The differences between these CPFEM and CPFFT results reveal that the two methods lead to different combinations of grain rotations and strain fields. Specifically, the results of these bicrystal simulations show that

- For the RZ-in-Goss bicrystal, figure 9, CPFFT gives higher strain gradients and more diverse rotations than the CPFEM model at low resolution (1 Fourier point or element in the RZ grain, 1×7 Fourier points or elements in the Goss grain). At higher resolution, the bicrystal starts to split up into fragments, becoming a polycrystal. The strain gradients and grain rotation diversity calculated by both methods are comparable at high resolution

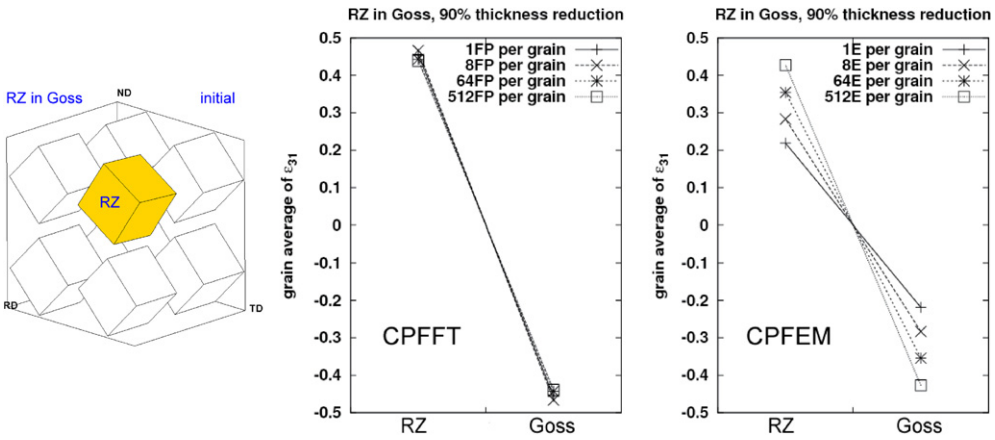

Figure 10. Plane-strain compression of a bicrystal (RZ in Goss) at 90% thickness reduction. The grain averages of strain component ϵ_{31} are plotted considering the different volume fractions of the crystals (for the RZ grain $\epsilon_{31} \times 1$, for the Goss grain $\epsilon_{31} \times 7$) for simulations run at different resolutions: 1, 8, 64, 512 Fourier points or elements in the RZ grain and 1×7, 8×7, 64×7, 512×7 Fourier points or elements in the Goss grain.

(512 Fourier points or elements in the RZ grain, 512×7 Fourier points or elements in the Goss grain).

- For the Cube$^{\sim}$-in-Goss case, figure 11, at low resolution, comparable strain gradients and grain rotations are obtained with CPFFT and CPFEM. As resolution increases, higher strain gradients and more diverse grain rotations are observed in the simulation results of both models. The differences in strain gradients between the CPFFT and CPFEM results become pronounced at high resolution.
- On average, the strain gradients across the bicrystals continuously rise with increasing resolution in CPFEM simulations, but hardly change in the CPFFT simulations, figures 10 and 12.

The CPFFT model calculates certain strain gradients at low resolution. The average strains can be captured even at the lower end of the resolution scale. This well explains why there is almost no resolution effect on the CPFFT simulation of the 1024 grain polycrystal in section 3. The CPFEM model gives the lowest strain gradient at low resolution. As resolution increases, the CPFEM simulations continuously approach higher strain gradients, and the calculated average grain strains grow accordingly. This explains why refined resolution strongly affects the CPFEM results.

We want to point out here that there is no real meaning in discussing the convergence of these bicrystal results as resolution increases, because, at large deformations, the crystals tend to split up, such that the initial bicrystal becomes different polycrystals in the simulations conducted at different resolutions.

5. Micro-texture predictions using the CPFFT model: results and discussion

One of the advantages of full-field models, such as CPFEM and CPFFT, over grain-cluster models is that they take into account the spatial configuration of the polycrystals and the grain interactions in the whole RVE [5, 7, 8, 43, 44]. This enables full-field models to predict intragranular reorientations during deformation. Although the related grain-cluster models

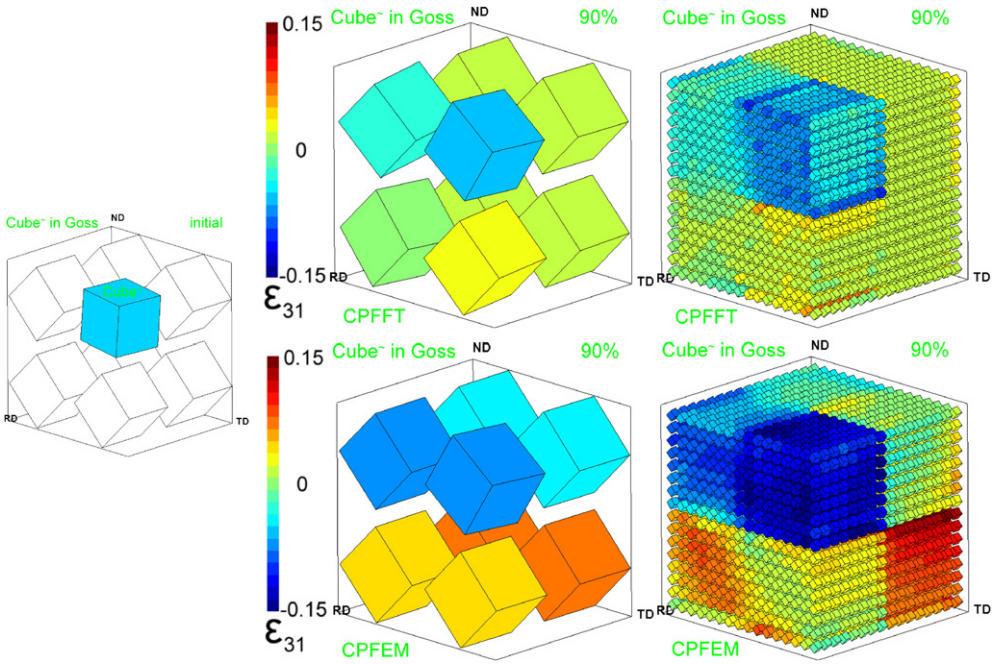

Figure 11. Final crystallographic orientations and strain states on the material points after plane-strain compression of a bicrystal (Cube˜ in Goss) at 90% thickness reduction. The cube symbols are rotated according to the final orientations, and colored according to the values of strain component ϵ_{31}. The results presented here are from the simulations run at the lowest resolution (1 Fourier point or element in the Cube˜ grain and 1×7 Fourier points or elements in the Goss grain) (left) and at the highest resolution (512 Fourier points or elements in the Cube˜ grain and 512×7 Fourier points or elements in the Goss grain) (right).

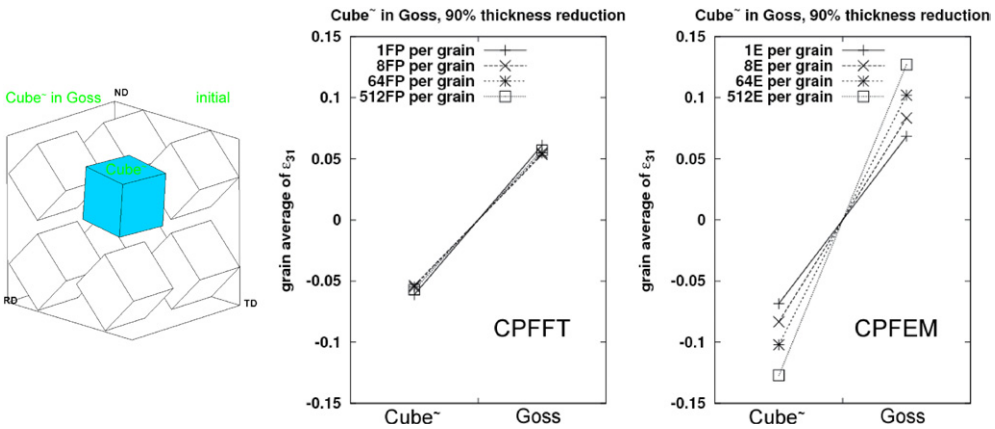

Figure 12. Plane-strain compression of a bicrystal (Cube˜ in Goss) at 90% thickness reduction. The grain averages of strain component ϵ_{31} are plotted considering the different volume fractions of the crystals (for the Cube˜ grain $\epsilon_{31} \times 1$, for the Goss grain $\epsilon_{31} \times 7$) for simulations run at different resolutions: 1, 8, 64, 512 Fourier points or elements in the Cube˜ grain and 1×7, 8×7, 64×7, 512×7 Fourier points or elements in the Goss grain.

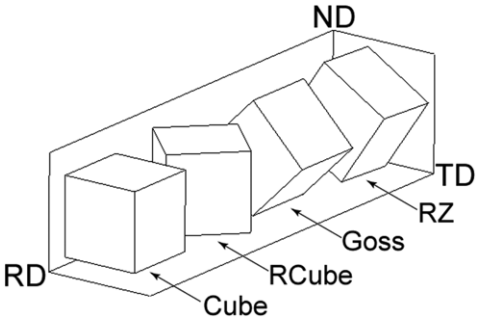

	φ_1	Φ	φ_2
Cube	0°	0°	0°
RCube	0°	0°	45°
Goss	0°	45°	0°
RZ	32°	85°	85°

Figure 13. Crystallographic orientations chosen to construct a 64-grain RVE.

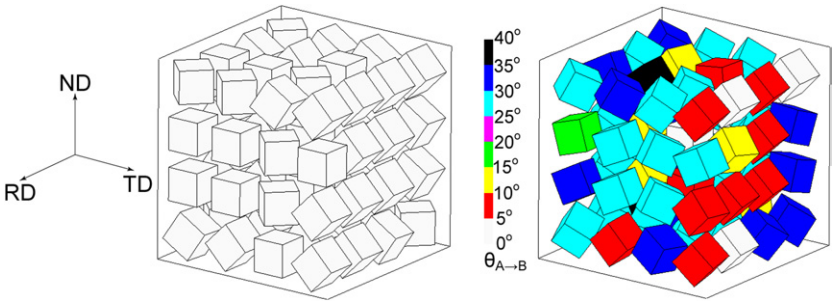

Figure 14. Crystallographic orientations of the 64-grain RVE before deformation (left) and after plane-strain compression at 90% thickness reduction (right) obtained in the case of one Fourier point per grain simulation. $\theta_{A\to B}$ is the misorientation between the starting orientation (A) and final orientation (B) for a single grain.

(e.g. GIA, ALAMEL) have been proven to be highly efficient for texture simulations, they have been less successful when applied at the single-crystal scale, as they do not account for the near- and far-field spatial arrangement of the crystals in the sample and the corresponding strain relaxations inside a wider cluster. When a single crystal is composed of more than one numerical unit, full-field models are able to simulate the orientation split-up inside one single grain [33, 42, 43, 45]. In the CPFFT model used in this work such split-up is due to grain interactions [33] while for the CPFEM model both intrinsic (grain interactions) and extrinsic mechanical conditions such as friction and complex externally imposed strain paths can enter the simulation, which in turn can lead to the fragmentation of originally homogeneously oriented grains [42, 45].

In this section we present a theoretical study on micro-texture evolution of a 64-grain RVE during plane-strain compression using the CPFFT approach. The sample is build up from four orientations (figure 13), arranged in random order (figure 14, left). The Cube, rotated Cube, Goss and RZ orientations have been chosen to study the initial orientation dependence and crystal neighbor influence of in-grain orientation split-up as analyzed earlier using CPFEM simulations in [42]. The choice of these four texture components is related to their different orientation stabilities under plane-strain loading [18, 42, 46, 47].

In previous CPFEM simulations on orientation stability, only single crystals and bicrystals have been investigated. In a 64-grain aggregate more grain-scale diversity is created by the grain neighborhood. The 50% thickness reduction used in the former study is extended to 90% in the current one. This is more revealing of the final stable texture components. The

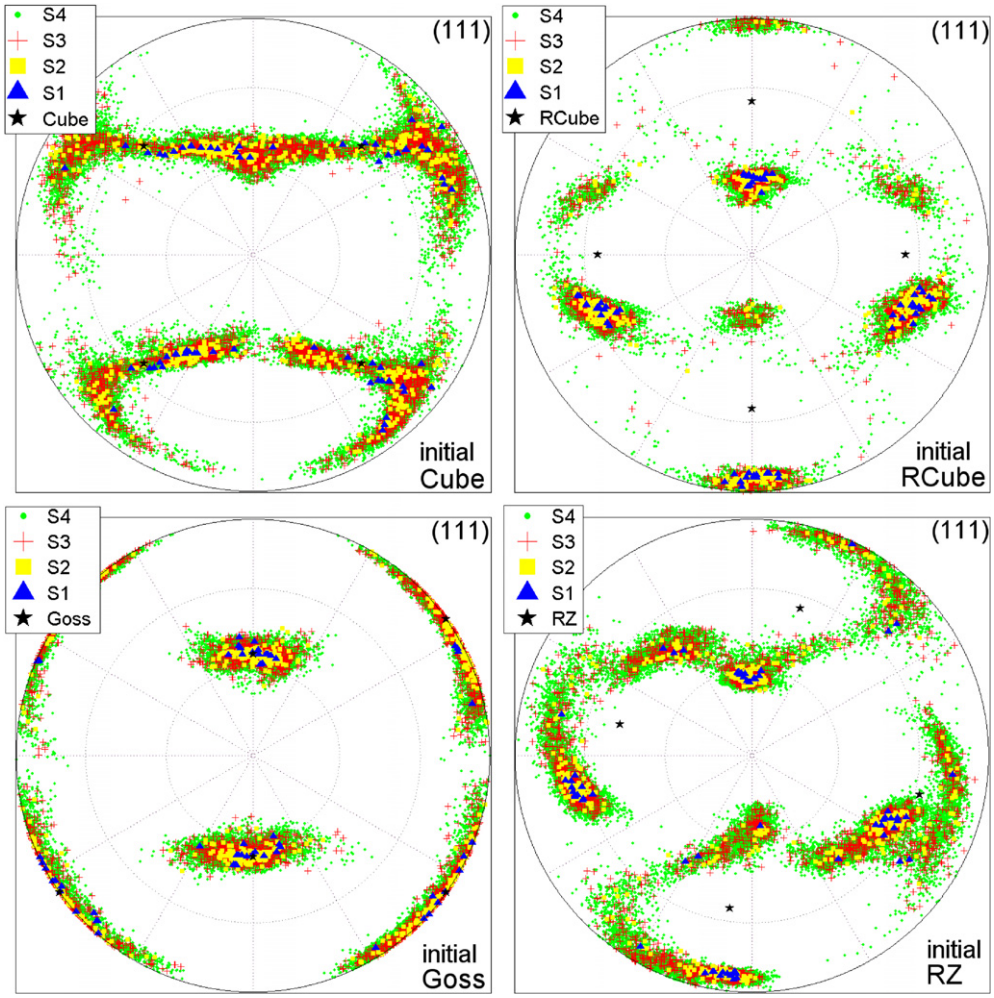

Figure 15. In-grain texture evolution inside the 64-grain RVE presented in the form of {1 1 1} pole figures. The split-up and resulting reorientation distribution is shown individually for the four selected initial texture components Cube, rotated Cube, Goss and RZ; CPFFT; plane-strain compression; thickness reduction 90%: S1 (1 Fourier point per grain simulation), S2 (8 Fourier points per grain simulation), S3 (64 Fourier points per grain simulation), S4 (512 Fourier points per grain simulation). The grains that have identical initial orientation are put into the same {1 1 1} pole figure, and the black stars mark the starting orientations.

simulations were run at four resolution levels, namely 1; 8($2 \times 2 \times 2$); 64($4 \times 4 \times 4$) and 512($8 \times 8 \times 8$) Fourier points per grain. The results of all simulations are shown in figure 15. Grains with identical initial orientation are presented in the same {1 1 1} pole figure. The black stars mark the starting orientations. The other markers are used to indicate the simulation results obtained at the different resolutions.

These results allow us to make a number of observations.

For the simulation with only one Fourier point per grain (marked by blue triangles in figure 15) the final orientation spread is due to the fact that the initially identically oriented grains have different neighbors in this 64-grain RVE. Depending on the initial orientation and grain neighborhood, the grain rotations can, hence, vary substantially. The results obtained for

Table 1. Misorientation ($\theta_{A\to B}$) between the starting orientation (A) and final orientation (B): statistics of 1 Fourier point per grain simulation (figure 14, right).

	$\max(\theta_{A\to B})$	$\min(\theta_{A\to B})$	$\text{mean}(\theta_{A\to B})$	$\Sigma(\theta_{A\to B})$ $(N = 16)$
Cube grains	38.4°	3.6°	21.0°	11.1°
RCube grains	33.3°	26.7°	29.0°	1.8°
Goss grains	22.9°	0.9°	8.8°	5.1°
RZ grains	34.5°	28.0°	30.0°	1.7°

Table 2. Misorientation ($\theta_{B\to C}$) between the final orientation (B) and the ideal texture component (C): statistics of 512 Fourier points per grain simulation; thickness reduction 90%.

	$\max(\theta_{B\to C})$	$\min(\theta_{B\to C})$	$\text{mean}(\theta_{B\to C})$	$\Sigma(\theta_{B\to C})(N = 16\times 512)$
Cube grains to Goss(C)	60.0°	4.0°	22.9°	7.6°
RCube grains to Copper(C)	55.0°	0.4°	8.5°	4.6°
Goss grains to Goss(C)	43.6°	0.2°	10.2°	6.9°
RZ grains to S(C)	46.1°	0.7°	15.6°	8.2°

the calculation with one Fourier point per grain are additionally presented in figure 14(right), to make a direct comparison with the starting orientations in figure 14(left), using the same method by sample-axis rotations and color-coded misorientations as in figure 3(right).

When divided by the macroscopic von Mises strain (2.645, at 90% thickness reduction), the misorientation $\theta_{A\to B}$ (between the starting and final orientations) can be used as a measure of the grain rotation rate, and its standard deviation $\Sigma(\theta_{A\to B})$ can be used to indicate the neighbor sensitivity of the rotation rate.

$$\Sigma(\theta) = \sqrt{\frac{1}{N}\sum_{i=1}^{N}[\theta - \text{mean}(\theta)]^2}.$$

The maximum, minimum, mean, and standard deviation of the rotation angles for initially differently oriented grains are listed in table 1. On average, the rotation rates $\dot{\theta}_{A\to B}$ follow the sequence $\dot{\theta}^{\text{RZ}}_{A\to B} > \dot{\theta}^{\text{RCube}}_{A\to B} > \dot{\theta}^{\text{Cube}}_{A\to B} > \dot{\theta}^{\text{Goss}}_{A\to B}$. Besides this global tendency, the rotation rates of Cube and Goss oriented grains are more sensitive to the influence of neighbor grains than those of RCube and RZ grains, following the sequence $\Sigma(\dot{\theta}^{\text{Cube}}_{A\to B}) > \Sigma(\dot{\theta}^{\text{Goss}}_{A\to B}) > \Sigma(\dot{\theta}^{\text{RCube}}_{A\to B}) \simeq \Sigma(\dot{\theta}^{\text{RZ}}_{A\to B})$.

For the simulations with more than one Fourier point in each grain, the intragranular misorientations are stimulated by the grain interactions. As it is shown in figure 15, at 90% thickness reduction, RCube oriented grains rotate into the copper orientation, RZ oriented grains rotate toward the S component, Cube grains rotate into the Goss orientation and Goss grains only rotate slightly. Based on these results we next calculated the misorientation ($\theta_{B\to C}$) between the simulated final orientations (B) and the closest ideal texture component (C) for the whole data set obtained from a simulation with 512 Fourier points per grain. From these misorientations we derived the maximum, minimum, mean and standard deviation as listed in table 2. The RZ and Cube grains show stronger intragranular orientation subdivisions than the Goss and RCube grains, as $\Sigma(\theta^{\text{RZ}}_{B\to C}) > \Sigma(\theta^{\text{Cube}}_{B\to C}) > \Sigma(\theta^{\text{Goss}}_{B\to C}) > \Sigma(\theta^{\text{RCube}}_{B\to C})$. We pick four initially differently oriented grains out of the 64-grain cluster from the 512 Fourier point per grain simulation. The final orientations of the Fourier points inside the

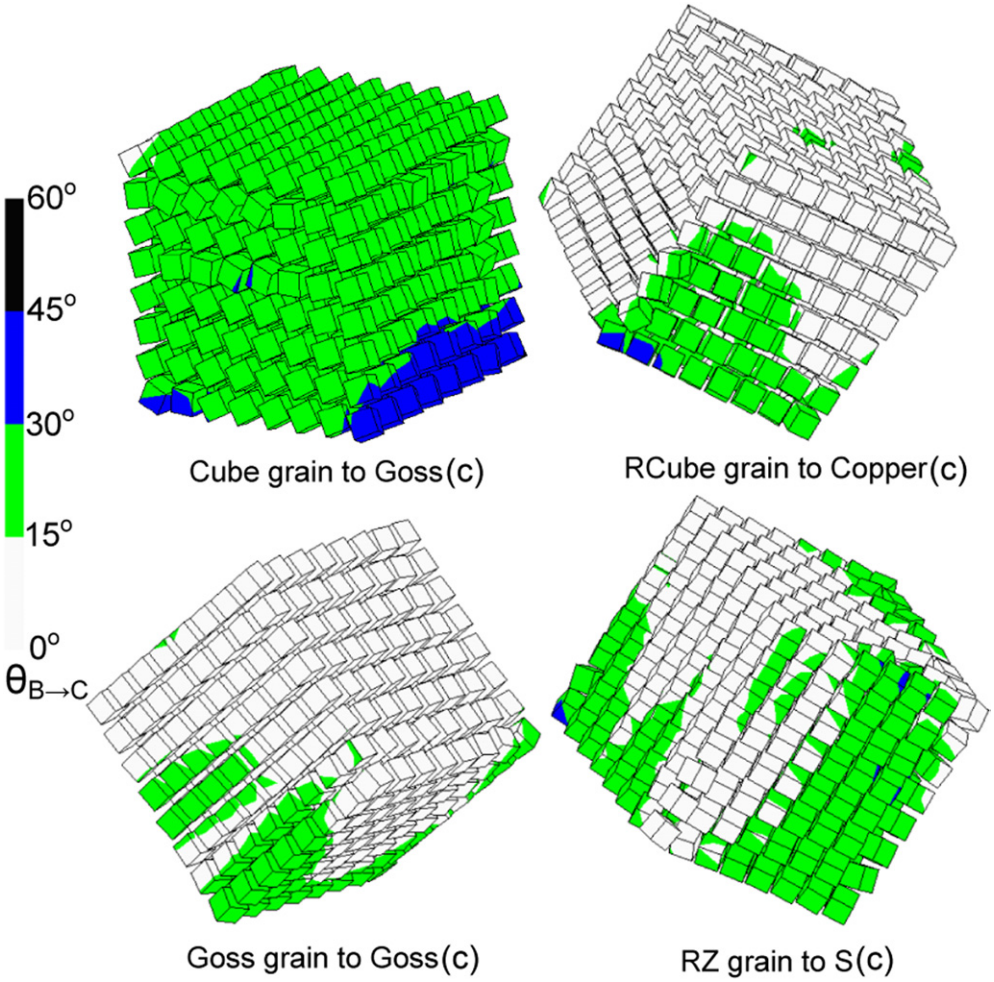

Figure 16. Example of in-grain orientation split-up in four grains inside the 64-grain RVE (512 Fourier points per grain calculation). $\theta_{B\to C}$ is the misorientation between the final orientation (B) and the ideal texture component (C). The reference ideal texture components (C) for initially differently oriented grains are given below the figures.

four grains are presented in figure 16 in terms of the small cube symbols. The material units (Fourier points) inside the initially Cube and RZ oriented crystals create upon loading more diverse in-grain rotation fields, than those inside the Goss grain. The RCube grains tend to split into two Copper components (equivalent under orthotropic sample symmetry). In figure 16, the misorientations between the final orientations and ideal texture components are color-mapped.

6. Conclusions

We simulated the statistical texture evolution of a FCC metal (plane-strain loading), and investigated the strain gradients predicted in bicrystals under the same deformation mode, with the full-field crystal plasticity Fast Fourier Transform and Finite Element models. Additionally

we conducted a grain-scale orientation fragmentation analysis using the FFT approach. The main conclusions are the following:

- Concerning the statistical texture evolution simulations of the 1024-grain ensemble:
  - In the CPFFT simulations Cube oriented grains show higher rotation rates away from their starting orientation and slower rotations at the later deformation stages toward stable plane-strain orientations (copper, S, brass) than in the CPFEM simulations.
  - With the same initial configuration and boundary conditions, using the same crystal plasticity constitutive equation and hardening law, the CPFEM and CPFFT simulations give different combinations of orientation and strain distributions.
- Concerning the strain gradient predictions in bicrystals:
  - The CPFFT model predicts certain strain gradients at low resolution. The average strains in the grains can be captured even at the lower end of the resolution scale. This explains that why there is nearly no resolution effect on the CPFFT simulation of the 1024 grain polycrystal.
  - The CPFEM model gives the lowest strain gradient at low resolution. As the resolution increases, the CPFEM simulations continuously approach higher strain gradients, and the calculated average strains in the grains grow accordingly. Thus, resolution strongly affects the CPFEM results.
- General comments on the texture predictions of the CPFFT and CPFEM models for engineering applications:
  - For the statistical texture evolution simulation with a sample size larger than one thousand grains like the ones in section 3, the orientation and strain distributions can be obtained at relatively low resolutions using the CPFFT model. For the CPFEM model, this would depend on the initial orientations inside the sample, which means higher resolution is needed when the initial orientation distribution tends to introduce higher strain gradients.
- Concerning micro-texture predictions of the 64-grain aggregate:
  - Plane-strain compression of the 64-grain RVE at 90% thickness reduction revealed that the RCube grains rotate toward the copper orientation; the RZ grains rotate close to the S orientation; the Cube grains rotate toward the Goss orientation; and the Goss grains only slightly rotate away from their initial orientation.
  - The rotation rates $\dot{\theta}_{A\to B}$ of grains with different initial orientations follow the following sequence: $\dot{\theta}^{\mathrm{RZ}}_{A\to B} > \dot{\theta}^{\mathrm{RCube}}_{A\to B} > \dot{\theta}^{\mathrm{Cube}}_{A\to B} > \dot{\theta}^{\mathrm{Goss}}_{A\to B}$.
  - The rotation rates of the Cube and Goss grains are more sensitive to the grain neighborhood than those of the RCube and RZ grains. The grain neighborhood dependence follows the sequence: $\Sigma(\dot{\theta}^{\mathrm{Cube}}_{A\to B}) > \Sigma(\dot{\theta}^{\mathrm{Goss}}_{A\to B}) > \Sigma(\dot{\theta}^{\mathrm{RCube}}_{A\to B}) \simeq \Sigma(\dot{\theta}^{\mathrm{RZ}}_{A\to B})$.
  - The Cube and RZ grains reveal larger in-grain rotation gradients after deformation than the Goss grains. The rotated Cube grains split into two equivalent copper components.

References

[1] Taylor G I 1938 *J. Inst. Metals* **62** 307–24
[2] Honeff H and Mecking M 1978 *Proc. ICOTOM 5 (Aachen, Germany)* ed G Gottstein and K Lücke (Berlin: Springer) p 265
[3] Van Houtte P 1981 *Proc. ICOTOM 6 (Tokyo, Japan)* ed S Nagashima (Japan: ISIJ) p 428
[4] Van Houtte P, Delannay L and Samajdar I 1999 *Textures Microstruct.* **31** 109

[5] Van Houtte P, Li S, Seefeldt M and Delannay L 2005 *Int. J. Plast.* **21** 589
[6] Evers L P, Parks D M, Brekelmans W A M and Geers M G D 2002 *J. Mech. Phys. Solids* **50** 2403
[7] Crumbach M, Pomana G, Wagner P and Gottstein G 2001 *Proc. 1st Joint Int. Conf. on Recrystallization and Grain Growth (Aachen, Germany)* ed G Gottstein and D A Molodov (Berlin: Springer) p 1053
[8] Schäfer C, Song J and Gottstein G 2009 *Acta Mater.* **57** 1026
[9] Eshelby J D 1957 *Proc. R. Soc.* A **241** 376
[10] Hill R 1966 *J. Mech. Phys. Solids* **14** 95
[11] Molinari A, Canova G R and Ahzi S 1987 *Acta Metall.* **35** 2983
[12] Lebensohn R A and Tomé C N 1993 *Acta Metall. Mater.* **41** 2611
[13] Peirce D, Asaro R J and Needleman A 1982 *Acta Metall. Mater.* **30** 1087
[14] Harren S V, Déve H and Asaro R J 1988 *Acta Metall. Mater.* **36** 2435
[15] Harren S V and Asaro R J 1989 *J. Mech. Phys. Solids* **37** 191
[16] Becker R 1991 *Acta Metall. Mater.* **39** 1211
[17] Becker R, Butler J F, Hu H and Lalli L A 1991 *Metall. Trans.* A **22** 45
[18] Beaudoin A J, Mecking H and Kocks U F 1996 *Philos. Mag.* A **73** 1503
[19] Sarma G B and Dawson P R 1996 *Int. J. Plast.* **12** 1023
[20] Sarma G B, Radhakrishnan B and Zacharia T 1998 *Comput. Mater. Sci.* **12** 105
[21] Mika D P and Dawson P R 1998 *Mater. Sci. Eng.* A **257** 62
[22] Bachu V and Kalidindi S R 1998 *Mater. Sci. Eng.* A **257** 108
[23] Sachtleber M, Zhao Z and Raabe D 2002 *Mater. Sci. Eng.* A **336** 81
[24] Zhao Z, Kuchnicki S, Radovitzky R and Cuitiño A 2007 *Acta Mater.* **55** 2361
[25] Zhao Z, Ramesh M, Raabe D, Cuitiño A and Radovitzky R 2008 *Int. J. Plast.* **24** 2278
[26] Moulinec H and Suquet P 1998 *Comput. Methods Appl. Mech. Eng.* **157** 69
[27] Michel J C, Moulinec H and Suquet P 2000 *Comput. Modeling Eng. Sci.* **1** 79
[28] Lebensohn R A 2001 *Acta Mater.* **49** 2723
[29] Mura T 1987 *Micromechanics of Defects in Solid* 2nd edn (Dodrecht: Martinus Nijhoff)
[30] Prakash A and Lebensohn R A 2009 *Modeling Simul. Mater. Sci. Eng.* **17** 064010
[31] Zeller R and Dederichs P H 1973 *Phys. Status Solidi* b **55** 831
[32] Lebensohn R A, Liu Y and Ponte Castañeda P 2004 *Acta Mater.* **52** 5347
[33] Lebensohn R A, Brenner R, Castelnau O and Rollett A D 2008 *Acta Mater.* **56** 3914
[34] Kalidindi S R, Bronkhorst C A and Anand L 1992 *J. Mech. Phys. Solids* **40** 537
[35] Kalidindi S R 2004 *Continuum Scale Simulation of Engineering Materials* ed D Raabe *et al* (Berlin: Wiely-VCH) p 529
[36] Roters F, Eisenlohr P, Hantcherli L, Tjahjanto D D, Bieler T R and Raabe D 2010 *Acta Mater.* **58** 1152
[37] Brown S B, Kim K H and Anand L 1989 *Int. J. Plast.* **5** 95
[38] Eisenlohr P and Roters F 2008 *Comput. Mater. Sci.* **42** 670
[39] Li S, Van Houtte P and Kalidindi S R 2004 *Modeling Simul. Mater. Sci. Eng.* **12** 845
[40] Press W H, Teukolsky S A, Vetterling W T and Flannery B P 1986 *Numerical Recipes* (Cambridge: Cambridge University Press)
[41] Engler O 2002 *Adv. Eng. Mater.* **4** 181
[42] Raabe D, Zhao Z, Park S-J and Roters F 2002 *Acta Mater.* **50** 421
[43] Raabe D, Zhao Z and Mao W 2002 *Acta Mater.* **50** 4379
[44] Eisenlohr P, Tjahjanto D D, Hochrainer T, Roters F and Raabe D 2009 *Int. J. Mater. Res.* **4** 500
[45] Raabe D, Sachtleber M, Zhao Z, Roters F and Zaefferer S 2001 *Acta Mater.* **49** 3433
[46] Hölscher M, Raabe D and Lücke K 1994 *Acta Mater.* **42** 879
[47] Raabe D, Zhao Z and Roters F 2004 *Scr. Mater.* **50** 1085